PHYSICS AND CHEMISTRY
OF SOLID STATE
V. 26, No.2 (2025) pp. 216-230

Section: Chemistry

DOI: 10.15330/pcss.26.2.216-230

Vasyl Stefanyk Precarpathian National University

ФІЗИКА І ХІМІЯ ТВЕРДОГО ТІЛА
Т. 26, № 2 (2025) С. 216-230

Хімічні науки

PACS: 81.20.Ka

ISSN 1729-4428 (Print)
ISSN 2309-8589 (Online)

Mariia Liaskovska[1,2], Tetiana Tatarchuk[3], Volodymyr Kotsyubynsky[4]

Structure, adsorption properties and Fenton-like catalytic activity of cobalt ferrite nanoparticles synthesized with Physalis extract

[1]Ivano-Frankivsk National Medical University, Ivano-Frankivsk, Ukraine; mliaskovska@ifnmu.edu.ua
[2]Department of Chemistry, Vasyl Stefanyk Precarpathian National University,
Ivano-Frankivsk, Ukraine; liaskovskam@gmail.com
[3]Educational and Scientific Center of Materials Science and Nanotechnology, Vasyl Stefanyk Precarpathian National University,
Ivano-Frankivsk, Ukraine
[4]Department of Applied Physics and Materials Science, Vasyl Stefanyk Precarpathian National University,
Ivano ‐Frankivsk, Ukraine; volodymyr.kotsuybynsky@pnu.edu.ua

Cobalt ferrite nanoparticles were synthesized from different parts of the *Physalis* plant. Characterization techniques including XRD analysis and FTIR data confirmed the spinel structure of the synthesized ferrites. According to the FTIR data, the spectra contain peaks corresponding to organic residues originating from the reducing agent. The data of XRD analysis indicate an increase in the lattice parameter and crystallite size in the order $CoFe_2O_4$–F < $CoFe_2O_4$–FH < $CoFe_2O_4$–H. According to the SEM observations, the $CoFe_2O_4$–H sample demonstrates a lower degree of agglomeration coupled with significant porosity, whereas the $CoFe_2O_4$–FH and $CoFe_2O_4$–F samples display more distinct lamellar structures. The inversion degree was calculated based on the Mössbauer spectra of the samples. The use of the physalis fruit+husk extract results in the formation of nanoparticles with an increased BET surface area (76 m^2/g), whereas using of physalis fruit extract results in the formation of an increased area of mesopores (46 m^2/g). The adsorption properties and Fenton-like catalytic activity of the synthesized samples have been investigated. The highest degree of Congo Red dye adsorption was observed for the sample $CoFe_2O_4$–FH while the lowest was for the sample $CoFe_2O_4$–H. FTIR spectra confirmed the chemosorption of the dye molecules onto the ferrite surface. The adsorption is higher on the surface with a higher degree of functionalization. The Fenton-like oxidation of Congo Red dye in the presence of H_2O_2 has been studied, demonstrating the high catalytic activity of all samples in dye removal and hydrogen peroxide decomposition. Amperometric I–τ curve measurements were used to observe the changes in the interactions between hydrogen peroxide and the ferrites.

Keywords: “green” synthesis; ferrite; adsorption; Fenton-like activity; electrochemical test; oxidative degradation.

Received 19 February 2024; Accepted 09 April 2025.

Introduction

The synthesis of nanoparticles using traditional synthetic materials leads to the formation of toxic waste and by-products that contribute significantly to environmental pollution [1]. A reliable alternative to these methods is «green synthesis» [2–6]. Such green methods include synthesis using various parts of plants [6], microorganisms [3], and biomaterials [7]. Green synthesis is less toxic and the synthesis products are safer, allowing them to be widely used for various environmental and biomedical applications [3]. It is known from the literature that the synthesis of nanoparticles using plant extracts makes nanoparticles biocompatible [7]. Namely, the presence of such components as flavonoids, carbohydrates, amino acids, polyphenols, carboxylic acids, tannins, and vitamins in the natural extracts lets to use them as reducing agents for nanoparticle synthesis [3].

The substances contained in plant extracts participate in redox reactions with metal salts and transform the latter into NPs with a predetermined morphology and size [3,8,9]. Moreover, these phytochemicals are not only reducing agents but also have an enveloping effect similar to surfactants, which prevent agglomeration of the obtained nanoparticles. The above-mentioned number of advantages in the formation of nanoparticles, as well as economic benefits, are factors that influenced the choice of the synthesis method [4].

The use of plant extracts [4] and biomaterials [9][10] for the synthesis of spinel nanoparticles has increased significantly in the last few years. For the synthesis of spinels, the following substances have been used: ginger root [11], honey [12,13], ginkgo biloba [5], aloe vera, okra extract [14], seaweed [15], Cydonia oblonga [8], limonia acidissima juice [16], jatropha-oil [17], sesame seed [18], curd [10] and other. All these bio- and phytomaterials have a unique composition and contain natural reducing agents.

Physalis is a perennial plant with a unique chemical composition that does not require special care during cultivation. This makes Physalis an ideal reductant for the green synthesis of the nanoparticles [19–23]. Most species of Physalis have a long history of use in folk medicine to treat various diseases [24]. Recently, the biological activities of extracts from different plant parts have been reported, which include antioxidants [25], anticancer [23] and anti-inflammatory [22]. The use of *Physalis alkekengi* as a reducing agent for the synthesis of nanoparticles is known [26], but it has not been used before for the synthesis of spinel ferrites. Velmurugan et al. [27] synthesized gold nanoparticles using *Physalis minima* plant extract. Flavonoids, phenols, and polyphenols contained in the extract were used as a reducing agent to create gold nanoparticles [27].

In this study, cobalt ferrite nanoparticles were synthesized using extracts of various parts of Physalis. The choice of *Physalis* as a "green" fuel agent is due to its chemical composition. In particular, ascorbic acid, caffeic acid, and terpenes (carotenes are tetraterpenes) are known for their reducing ability [28], which allows *Physalis* to be used not only as a fuel but also as a reducing agent. Physalis fruits contain citric, malic, tartaric, succinic, caffeic, ferulic, and sinapic acids; vitamin C; carbohydrates; tannins; carotene; physalin and pectin. The flowers of *Physalis* contain carotenoids: physalin A and physalin B [19–21]. The presence of these substances, together with the ease of cultivation, determine the choice of *Physalis* as a "green" fuel agent in the formation of spinel ferrite.

I. Experimental

1.1. Physalis extract preparations

The husk and fruits of physalis have been used to obtain extracts. To prepare the extracts, the selected part of physalis is mixed with distilled water in a ratio of 1:2, then boiled for 10 minutes. This mixture is kept in a thermos for 24 hours before filtering the extracts. The filtered extracts are then stored in a refrigerator at 4°C. In total, three varieties of extracts have been prepared: one from the husk, one from both the fruit and husk, and one solely from the fruit. These extracts have been employed for the synthesis of nanoparticles.

1.2. Synthesis of $CoFe_2O_4$ NPs

Cobalt ferrite was synthesized through the 'green' sol-gel method followed by auto-combustion using $Co(CH_3COO)_2 \cdot 4H_2O$ and $Fe(NO_3)_3 \cdot 9H_2O$ reagents (Fig. 1). First of all, a mixture of metal salts was dissolved in 50 mL of distilled water. The solutions were mixed for 30 min at a temperature of 45°C. Then 50 mL of the extract of *Physalis* husk (H), fruit+husk (FH), or fruit (F) was added as eco-friendly fuel agent. The resulting mixture was stirred at a constant temperature for 30 min.

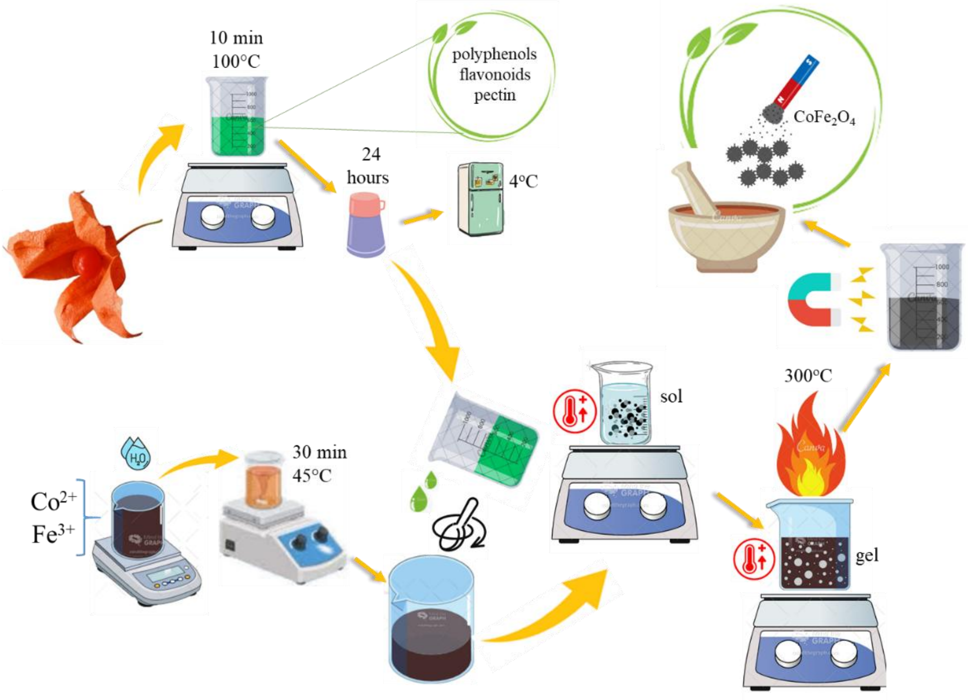

Fig. 1. Schematic synthesis of $CoFe_2O_4$ using the *Physalis* extracts.

The solution was subsequently placed on a hot plate to facilitate the formation of a sol. Following this, the mixture was transformed into gel until auto-combustion of the gel occurred. The obtained products $CoFe_2O_4$–H, $CoFe_2O_4$–FH, and $CoFe_2O_4$– F were ground in a mortar, resulting in fine powders.

1.3. Characterization techniques

The X-ray diffraction analysis has been performed using a Shimadzu XRD-7000 X-ray with $Cu_{K\alpha}$ monochromatic radiation source ($\lambda = 1.5418$ Å). The crystal phases were identified using the Match! 3.0/FullProf software. FTIR analysis was performed using a Nicolet Nexus 470 spectrometer (Thermo Scientific) in the range of 4000–400 cm^{-1} with a number of scans of 128 and a resolution of 4 cm^{-1}. The surface morphology of the samples was studied with a REMMA-102-02 scanning electron microscope (JCS SELMI, Ukraine) with an attachment for energy-dispersive analysis (EDS). The accelerating voltage is approximately 20.00 kV. The textural analysis has been carried out using N_2 adsorption/desorption isotherms obtained at 77 K using an automatic Quantachrome sorption analyzer. The samples were degassed overnight at 180°C before each measurement. The calculations of surface area, pore volume, pore size distribution, and pore diameter were performed using Quantachrome NovaWin software (v.11.04). Mössbauer spectra were recorded using an MS1104Em spectrometer in transmission geometry with a moving absorber and a $^{57}Co(Cr)$ radiation source. The isomeric shift was calibrated relative to α-Fe, and the velocity resolution was approximately 0.01 mm/s per channel. The resulting spectra had signal-to-noise ratios exceeding 31. All measurements were conducted at room temperature, and the spectra were analyzed using UnivemMS 7.01 software.

1.4. The adsorption/catalytic experiments

The adsorption experiments were conducted using batch mode. Congo Red dye as a model pollutant has been used to examine the adsorption properties of ferrites. 20 mg of the adsorbent was inserted into 20 mL of a dye solution at different concentrations (10, 20, 50, 75, and 100 mg/L). The mixture was shaken at 25°C for 24 hours to reach adsorption equilibrium. Then magnet was used to remove the adsorbent. Thereafter, the equilibrium concentrations (C_e) of the dye within the solutions were calculated by measuring the absorbance at a wavelength of 500 nm, utilizing a ULAB-102UV spectrophotometer. The adsorption capacity (mg/g) was calculated with the following equation: $q_{ads} = (C_o – C_{eq})\cdot V/m$, where C_o is the initial concentration of the CR dye, mg/L; C_e is an equilibrium concentration of CR dye, mg/L; m is the adsorbent mass, mg; V is the solution volume, L. The dye removal (in %) was calculated by the formula: $Removal(\%) = [(C_o – C_{eq})/C_o]\cdot 100\%$.

The Fenton-like oxidation of CR was conducted by placing 120 mg of the catalyst into 40 mL of a Congo Red dye solution ($[CR]_0$=10 mg/L). Then H_2O_2 (20 mM) was added to the solution after 30 minutes (the time for reaching the adsorption equilibrium). The experiment was also repeated without the adsorption equilibrium stage. The experiment was also performed without the adsorption equilibrium stage to conclude the role of the adsorption in the catalytic wet peroxide oxidation of CR. The dye concentrations in the solutions were measured with a ULAB-102UV spectrophotometer at 500 nm. The residual concentration of H_2O_2 was measured at a wavelength of 470 nm by UV-vis spectrophotometry using the metavanadate method.

1.5. Electrochemical tests

Amperometric I–τ curves were obtained using an electrochemical workstation galvanostat-potentiostat Autolab PGSTAT12 Eco Chemie. The electrode cell consisted of three electrodes: a saturated Ag/AgCl electrode as the reference electrode, a Pt foil as the counter electrode, and a working electrode (ferrite-coated FTO). The working electrode was prepared using the ferrite aqueous solution, which was coated on the FTO glass (1.4 cm × 3 cm). After each coating, the electrode was sintered at 90°C for 15 min. The solution of Congo Red dye ([CR] = 10 mg/L) was used as an electrolyte. Hydrogen peroxide solution ($[H_2O_2]$ = 20 mM) was used as an activator of current transmission. H_2O_2 solution was added drop-wise at continuous stirring and I–τ curves were recorded.

II. Results and discussion

2.1. XRD analysis

The XRD patterns of $CoFe_2O_4$ samples, synthesized using different plant sources (Fig. 2a), confirm the formation of a pure spinel phase. All samples are identified as single-phase materials belonging to the Fd3m space group. The sharp diffraction peaks indicate good crystallinity of the samples.

Variations in the lattice parameter and crystallite sizes are observed and are closely related to the type of extract. The lattice parameters of the samples exhibit a clear trend, increasing in the order
$CoFe_2O_4$–F < $CoFe_2O_4$–FH < $CoFe_2O_4$–H (Fig. 2b). The $CoFe_2O_4$–H sample demonstrates the highest lattice parameter (8.371±0.002 Å), while the $CoFe_2O_4$–F sample has the lowest lattice parameter (8.339±0.006 Å). This variation can be attributed to the activity of the reductant (fuel) used during the synthesis. A more active reductant results in higher synthesis temperatures, which promote thermal expansion of the crystal lattice and, consequently, results in larger lattice parameters. The crystallite size analysis (Fig. 2b) shows that the smallest crystallites are formed in the $CoFe_2O_4$–F sample. This suggests that the use of fruit extract as a reductant slows down crystal growth, resulting in smaller crystallite sizes. Conversely, the $CoFe_2O_4$–H sample exhibits the largest crystallite size, which correlates with the higher synthesis temperature caused by a more active reductant. Thus, higher synthesis temperatures promote lattice expansion and crystallite growth, while lower temperatures and less active reductants result in smaller crystallites and more compact structures.

2.2. Scanning Electron Microscopy (SEM) and energy-dispersive spectroscopy (EDS).

Fig. 3a presents the surface morphology of $CoFe_2O_4$

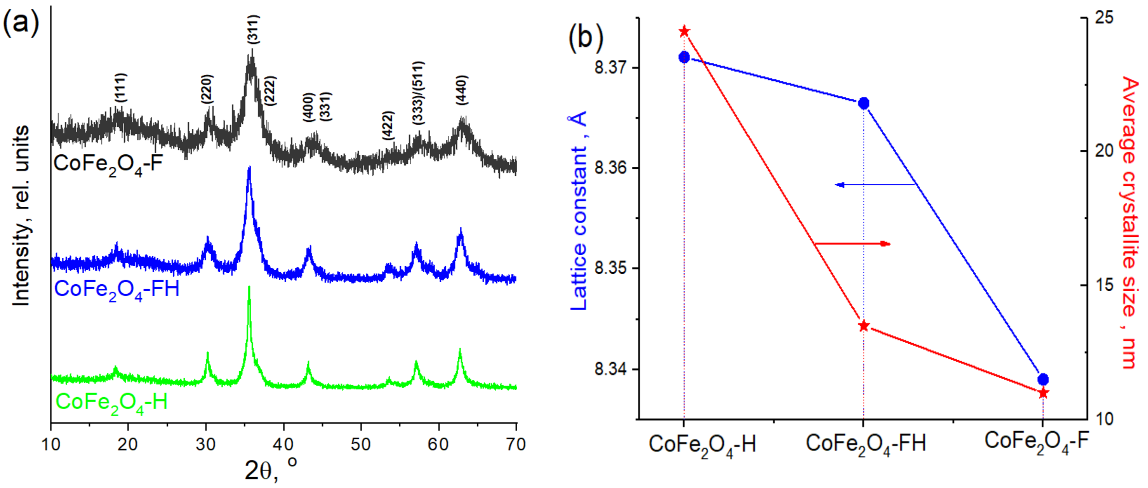

Fig. 2. (a) XRD patterns and (b) lattice constant and average crystallite size changes of cobalt ferrites, synthesized using different parts of physalis (H is Physalis husk; FH is Physalis fruit+husk; F is Physalis fruit).

samples analyzed through scanning electron microscopy (SEM) images. The samples tend to form agglomerated particles; however, the $CoFe_2O_4$–H sample demonstrates a lower degree of agglomeration coupled with significant porosity. In contrast, the $CoFe_2O_4$–FH and $CoFe_2O_4$–F samples display more distinct lamellar structures.

The observed morphology underscores the influence of the plant extract, which may serve not only as a reducing agent and fuel but also as a surfactant that mitigates particle adhesion during the synthesis process. Energy-dispersive spectroscopy results, as shown in Fig. 3b, prove the presence of iron, cobalt, and oxygen chemical elements. The elemental composition, expressed in weight percent and depicted in Table 1, aligns with the theoretically predicted values.

2.3. Mössbauer spectroscopy

The spectra measured for materials synthesized using Physalis husk (H) and Physalis fruit and husk (FH) exhibit a central doublet and broadened sextets, indicating the presence of both ferromagnetic and superparamagnetic ferrite particles. At the same time spectra of material synthesized using Physalis fruit (F) consist of symmetric paramagnetic doublet only. The transition of particles to a single-domain state results in thermal oscillation of the magnetic moment between the easy magnetization axes. Superparamagnetic relaxation is observed when the average time between two magnetic moment flips (Neel relaxation time, τ_N) becomes shorter than the measurement time, defined by the lifetime of the ^{57}Fe nucleus in its excited state (τ=141.8 ns). The Neel time can be estimated as $\tau_N = \tau_0 exp\left(\frac{K_{eff}V}{kT}\right)$, where $\tau_0 \approx 10^{-9}$–10^{-10} s is the characteristic relaxation time (intrinsic time scale of the system that corresponds to the frequency of attempts for a magnetic moment to flip between energy states and depends on the material's magnetic anisotropy and the gyromagnetic properties of the nanoparticles), K_{eff} is an effective magnetocrystalline anisotropy constant, V is a volume of a nanoparticle, T is a temperature. Higher anisotropy leads to longer τ_0, as it requires more energy to overcome the energy barrier for magnetic moment flipping but smaller particles exhibit faster relaxation (shorter τ_0). As a result, the product $K_{eff}V$ is in the range of $(1.1$–$2.1)\cdot 10^{-20}$ J. The effective values of magnetocrystalline anisotropy (K_{eff}) depend on the particles and for $CoFe_2O_4$ nanoparticles with an average size of 9 nm is $1.8\cdot 10^4$ J/m^3 [29]. The values of K_{eff} =(1–5)$\cdot 10^4$ J/m^3 were calculated for $CoFe_2O_4$ in [30] for ferrite particles with the sizes 5–6 nm. A close value of $2.5\cdot 10^4$ J/m^3 was obtained by [31] for $CoFe_2O_4$ nanoparticles with a size of about 3 nm. Assuming K_{eff} =$3\cdot 10^4$ J/m^3 it can estimate the particle size that corresponds to the transition from magnetically ordered state to superparamagnetic in a range of 9–11 nm (spherical particle approximation). Mössbauer spectra of the $CoFe_2O_4$–F sample consist of doublet only so there is no particle fraction in which a magnetically ordered state is possible at room temperature. The obtained value is in good agreement with the results of the $CoFe_2O_4$–F ferrite particle size estimation from XRD data.

The experimental spectra of $CoFe_2O_4$–H and $CoFe_2O_4$–FH samples (Fig. 4) were optimally fitted by a superposition of four six-line magnetic subspectrums, three of which correspond to Fe^{3+} ions in tetrahedral A positions and the fourth subspectrum corresponds to octahedrally coordinated Fe^{3+} ions. The number of used sextet components was based on the calculations of probabilities of various ion surroundings for Fe^{3+} in the cobalt ferrite structure [32]. Each sextet component represents Fe^{3+} ions placed in specific tetrahedral (A) or octahedral (B) sites, where their hyperfine magnetic fields are influenced by the surrounding cationic arrangement. The association of Fe^{3+} ions with tetrahedral sublattice was done using criteria of respectively lower isomeric shift values due to stronger covalence Fe_A–O bonds [8]. The spectrum of the $CoFe_2O_4$–F sample was described as a symmetric doublet only (Fig. 4). The obtained results are summarized in Table 2.

It is known that the ferrites with a spinel structure (Fd3m) follow the general formula $(Me^{2+}_yFe^{3+}_{1-y})_A[Me^{2+}_zFe^{3+}_{2-z}]_BO_4$, where Me^{2+} (in our case, Co^{2+}) and Fe^{3+} cations occupy tetrahedral (A) and octahedral (B) sites in the face-centered cubic lattice formed by oxygen ions. The inversion degree (z)

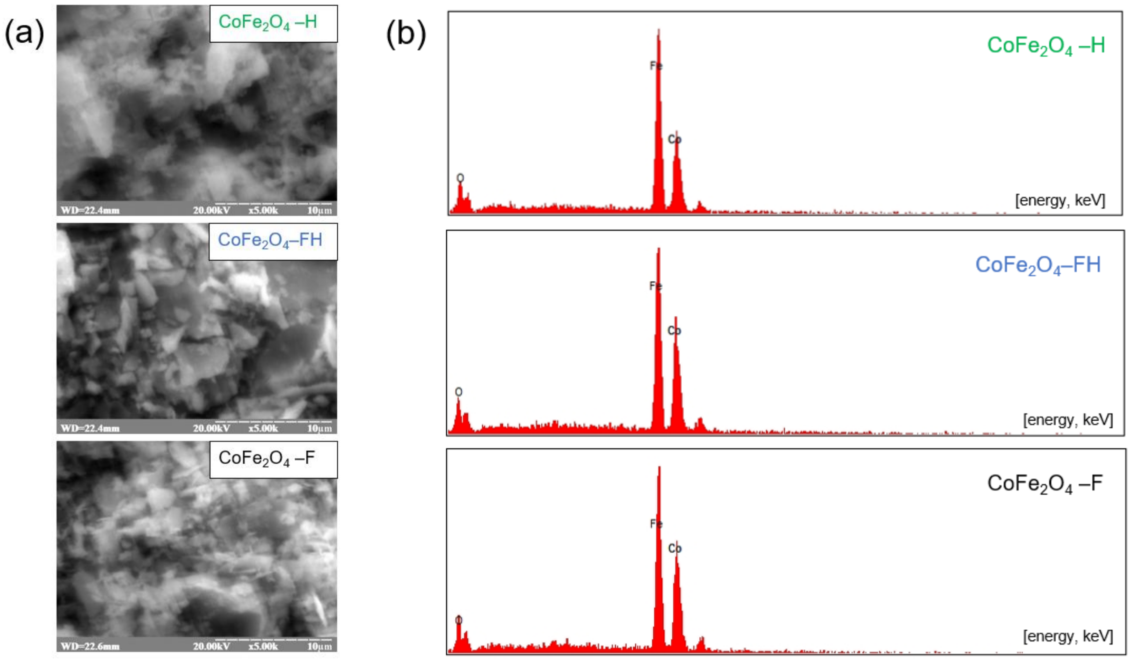

Fig. 3. (a) SEM images of CoFe$_2$O$_4$ NPs; (b) The EDS analysis of cobalt ferrites.

Table 1.

The element composition of CoFe$_2$O$_4$, calculated from EDS analysis data

Sample	at. %			
	Co	Fe	O	Total
CoFe$_2$O$_4$–H	9.78	21.02	69.2	100
CoFe$_2$O$_4$–FH	11.95	19.47	68.58	100
CoFe$_2$O$_4$–F	12.73	18.92	68.35	100

Table 2.

The Mössbauer spectra parameters of CoFe$_2$O$_4$ ferrites synthesized using different parts of physalis (H is Physalis husk; FH is Physalis fruit and husk; F is Physalis fruit): I$_S$ is isomeric shift; Q$_S$ is quadrupole splitting; H is hyperfine field; S is relative integral intensity; G is line width)

	Site	Is, mm/s	Qs, mm/s	H, kOe	S, %	G, mm/s
CoFe$_2$O$_4$–H						
1	A1	0.26	-0.08	458.4	4.3	0.30
2	A2	0.30	-0.02	483.7	28.6	0.60
	A3	0.26	-0.05	436.7	13.8	0.73
	B1	0.39	0.06	394.5	45.5	1.64
	D	0.30	0.71	–	7.8	0.51
	CoFe$_2$O$_4$–FH					
1	A1	0.34	-0.09	504.2	3.3	0.33
2	A2	0.27	0.01	468.0	19.7	0.56
	A3	0.29	-0.01	486.8	14.7	0.49
3	B1	0.38	-0.03	422.1	43.1	1.40
4	D	0.33	0.70	–	19.2	0.51
CoFe$_2$O$_4$–F						
1	D	0.33	0.78	–	100	0.57

represents the fraction of divalent cations located in the B sites, and for bulk CoFe$_2$O$_4$ z is typically close to 1 [32]. For ferrite nanoparticles, the inversion degree is influenced by surface energy, lattice strain, and synthesis conditions. These factors lead to a partial redistribution of Co^{2+} and Fe^{3+} ions, deviating from the inversion degree observed in bulk material. The changes in z affect the magnetic and catalytic properties of nanosized ferrites, making their cation distribution highly dependent on particle size and preparation methods. The cation distribution plays a crucial role in determining the magnetic and catalytic properties of spinel ferrites, which are influenced by synthesis conditions and subsequent thermal treatments.

The inversion degree and distribution of Co^{2+} ions between tetrahedral (A) and octahedral (B) coordinated sites were determined through a combination of Mössbauer spectra analysis and EDS data (Table 2)

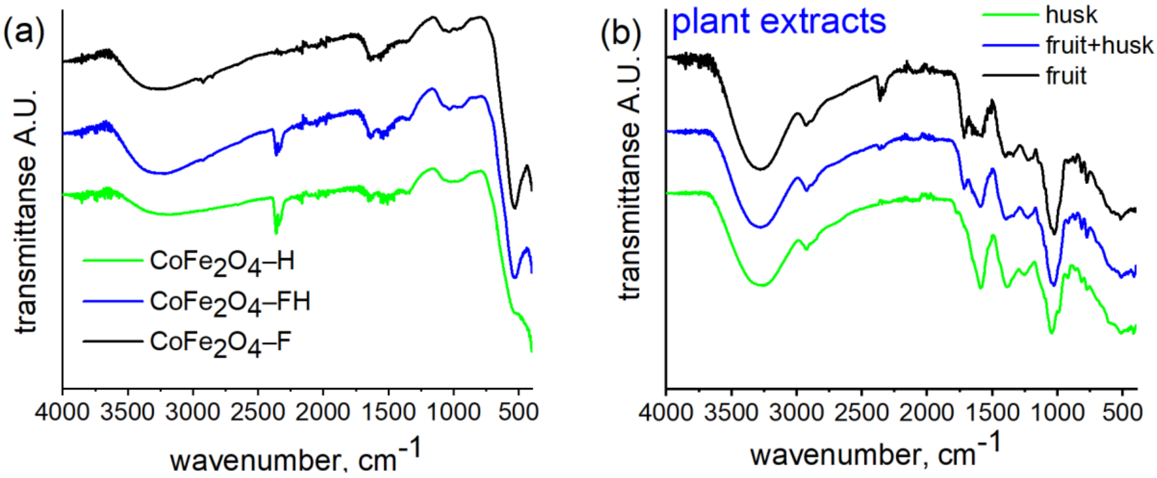

Fig. 5 The FTIR-ATR spectra of (a) $CoFe_2O_4$ samples and (b) the extracts of *Physalis* husk, fruit+husk, and fruit, which were used as a “green” agent.

according to [32]. EDS data about Co/Fe molar ratios were denoted as K1. Mossbauer data about the ratio between tetrahedrally and octahedrally surrounded Fe^{3+} ions (Fe_A/Fe_B) were denoted as K3. The solving of equations (y+z)/(3-y-z)=K1 and (1-y)/(2-z)=K3 allows to calculate inversion degree z for $(Me^{2+}_{y}Fe^{3+}_{1-y})_A[Me^{2+}_{z}Fe^{3+}_{2-z}]_BO_4$ structure. The values of the K1 parameter were determined as 0.49, 0.65, and 0.71 for $CoFe_2O_4$–H, $CoFe_2O_4$–FH, and $CoFe_2O_4$–H, respectively. Unfortunately, the calculation of the inversion degree is possible for $CoFe_2O_4$–H and $CoFe_2O_4$–FH samples only due paramagnetic nature of the $CoFe_2O_4$–F sample. The values of the K3 parameter were calculated as 1.03 and 0.87 for $CoFe_2O_4$–H and $CoFe_2O_4$–FH samples. Thus, the calculated cation distributions are $(Fe^{3+})_A[Co^{2+}_{1.00}Fe^{3+}_{1.00}]_BO_4$ and $(Co^{2+}_{0.15}Fe^{3+}_{0.85})_A[Co^{2+}_{0.85}Fe^{3+}_{1.15}]_BO_4$ for $CoFe_2O_4$–H and $CoFe_2O_4$–FH samples.

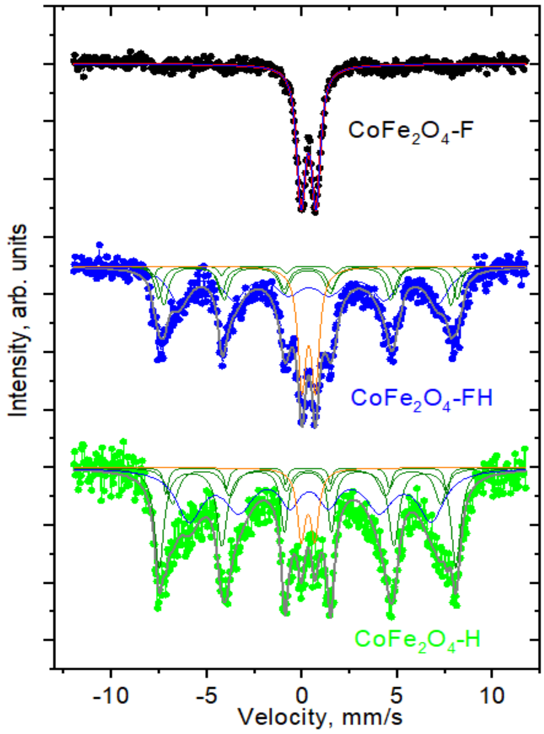

Fig. 4. Mössbauer spectra of cobalt ferrites samples synthesized using different parts of physalis (H is Physalis husk; FH is Physalis fruit and husk; F is Physalis fruit).

2.4. IR spectroscopy

Fig. 5a shows the FTIR spectra of the synthesized $CoFe_2O_4$ samples. The tetrahedral M–O bond is characterized by bands at 530 cm^{-1}, 528 cm^{-1}, and 505 cm^{-1} for samples FH, F, and H respectively. Force constants for the tetrahedral site were calculated by the formula $K_T = 4\pi^2 c^2 \nu^2 \mu$ [8] and are listed in Table 3. The band corresponding to the octahedral M–O bond is usually placed at around 400 cm^{-1}, which is beyond the limit of detection for the instrument used. The presence of O–H bonds is confirmed by the broad band in the range of 3600–3100 cm^{-1} and correlates with the FTIR spectra for the extracts used (Fig. 5b). The spectra of the $CoFe_2O_4$–H and $CoFe_2O_4$–FH samples demonstrate the absorption band at 2360–2333 cm^{-1}, which is attributed to the presence of adsorbed CO_2. The region between 1250 cm^{-1} and 900 cm^{-1} contains typical bands for phenolic compounds, sugars, organic acids, and nitrogenous substances, such as the vibration of C–O, C–C, C–N, and C–H bonds [33,34]. Furthermore, the region 1980–1350 cm^{-1} indicates vibrational stretching of double bonds, which are characteristic of organic residues in the samples. The umbrella mode at 1340–1070 cm^{-1} indicates the presence of $–CH_3$ functional groups and is related to the stretching of C–C and C–O bonds. This indicates the presence of biocomponent residues from the extract on the surface of the synthesized nanoparticles. The band between 1100 cm^{-1} and 780 cm^{-1} (Fig. 5b) can be attributed to the C–O stretching in phenolic compounds, the C–H deformation of the $–CH_3$ and $=CH_2$ groups, and to the anti-symmetrical −COO stretching of esters [27,33,34].

Table 3.

IR absorption bands, corresponding to tetrahedral sites, and force constants.

Parameters	$CoFe_2O_4$–H	$CoFe_2O_4$–FH	$CoFe_2O_4$–F
ν_T, cm^{-1}	505	530	528
$K_T \times 10^4$, dynes/cm^2	2.34	2.58	2.56

2.5. Surface area and pore volume

The nitrogen adsorption-desorption isotherms of synthesized cobalt ferrites are presented in Figs. 6a–c. These isotherms are indicative of mesoporous materials because they exhibit a hysteresis loop that is categorized as type IV, according to the IUPAC classification [35]. The surface area is increased in the row $S_{BET}(CoFe_2O_4–F) = 62 m^2/g$ $S_{BET}(CoFe_2O_4–H) =$ $= 69\ m^2/g < S_{BET}(CoFe_2O_4–FH) = 76\ m^2/g$ (Table 4). The pore size distribution and cumulative surface area of $CoFe_2O_4$, synthesized with various "green agents", are depicted in Figs. 76d–f. The pore volume is highest for the $CoFe_2O_4$–FH sample (0.105 cm^3/g), whereas for $CoFe_2O_4$–H and $CoFe_2O_4$–F samples it equals 0.079 and 0.100 cm^3/g (Table 4). For the synthesized samples a cardinal difference is observed in the values of the micro- and mesopore areas. The mesopore area increases in the row H–FH–F and is 17 m^2/g for $CoFe_2O_4$–H, 34 m^2/g for the sample $CoFe_2O_4$–FH, and 46 m^2/g for $CoFe_2O_4$-F. The micropore area increases in row F < FH < H and is 52 m^2/g for the sample $CoFe_2O_4$–H, 42 m^2/g for the sample $CoFe_2O_4$–FH, and 16 m^2/g for the sample $CoFe_2O_4$–F. The sample $CoFe_2O_4$–H is a microporous material, while the samples $CoFe_2O_4$–F and $CoFe_2O_4$–FH have pronounced mesoporosity. The pore radii, calculated by DFT method, are increased in the row $CoFe_2O_4$–F (1.8 nm) < $CoFe_2O_4$–H (1.9 nm) < $CoFe_2O_4$–FH (2.4 nm) (Table 4).

2.6. Adsorption properties

The surface charge of ferrites was investigated by measuring a point of zero charge (pH_{PZC}) in an aqueous solution. The point of zero charge (pH_{PZC}) helps to predict the ability of a surface to electrostatically attract or repel ions and molecules depending on the nature of the pollutant. Fig. 7 shows that the surface charge (pH_{PZC}) of cobalt ferrites largely depends on the nature of the reducing agent. The point of zero charge (pH_{PZC}) increases in the order $CoFe_2O_4$–FH < $CoFe_2O_4$–H < $CoFe_2O_4$–F and scales 7.74, 7.79, and 7.84, respectively.

Fig. 8a illustrates the adsorption isotherms of studied cobalt ferrites towards the Congo Red dye as a model pollutant [36,37]. Figs. 8b and 8c show linearized adsorption isotherms according to Langmuir and Freundlich models. The parameters of the abovementioned adsorption models are listed in Table 5. It can be seen that the adsorption capacity is increased in the row

$q_{ads}(CoFe_2O_4–H) = 18.42$ mg/g $< q_{ads}(CoFe_2O_4–F) =$
$= 31.85$ mg/g $< q_{ads}(CoFe_2O_4–FH) = 38.46$ mg/g

(Table 5). The same trend is observed for Langmuir constant K_L, which is highest for the $CoFe_2O_4$–FH sample

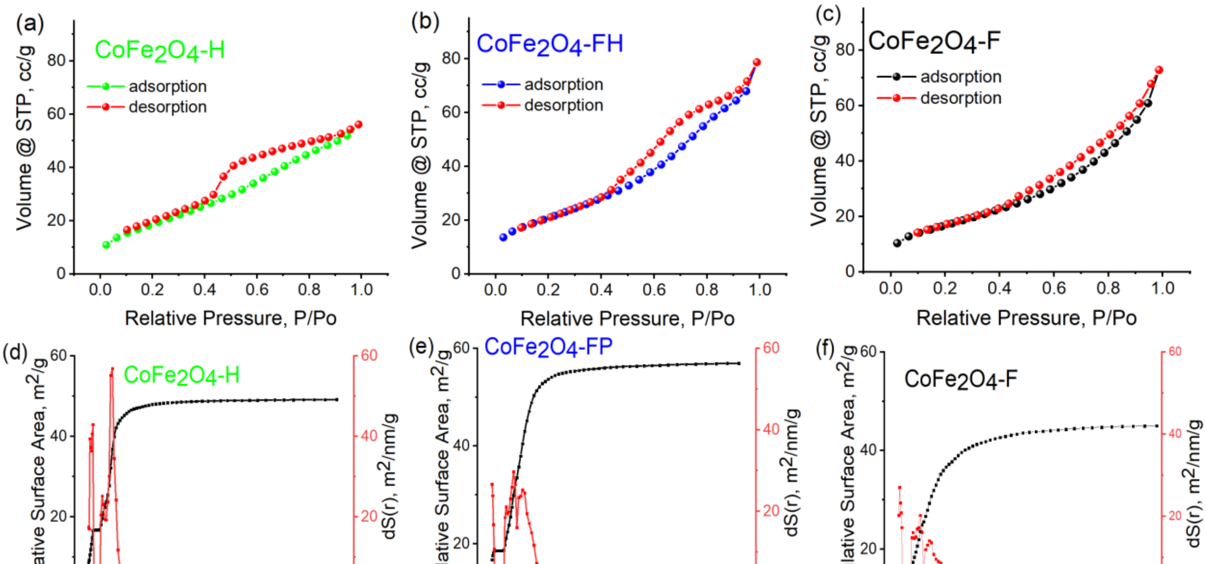

Fig. 6. (a–c) N_2 adsorption-desorption isotherms and (d–f) pore size distribution and cumulative surface area of $CoFe_2O_4$, synthesized with various "green agents".

Table 4.

The textural parameters of $CoFe_2O_4$, synthesized using various parts of Physalis.

Parameter	Sample		
	$CoFe_2O_4$–H	$CoFe_2O_4$–FH	$CoFe_2O_4$–F
S_{BET}, m^2/g	69	76	62
S_{meso}, m^2/g	17	34	46
S_{micro}, m^2/g	52	42	16
V, cm^3/g	0.079	0.105	0.100
V_{meso}, cm^3/g	0.025	0.051	0.078
V_{micro}, cm^3/g	0.054	0.054	0.022
R_{DFT}, nm	1.9	2.4	1.8

(K_L=0.21 L/mg) and the lowest for the $CoFe_2O_4$–H sample (K_L=0.12 L/mg). Therefore, the presence of organic species, originating from the extracts, on the $CoFe_2O_4$ surface strengthens the interaction between the Congo red dye molecules and the adsorbent surface. In addition, Table 5 shows the values of the Freundlich constant K_F, which are increased in the row K_F($CoFe_2O_4$–H) = 9.3 (mg/g)(mg/L)^n < K_F($CoFe_2O_4$–F) = 9.13 (mg/g)(mg/L)^n < K_F($CoFe_2O_4$–FH) = 10.7 (mg/g)(mg/L)^n (Table 5). The R^2 value for both adsorption models indicates the best fitting for the Langmuir model and, thus, the prevalence of monomolecular interactions of CR dye molecules with adsorbent surface. Fig. 8d demonstrates the adsorption removal of dye from an aqueous. The highest degree of dye removal was for sample $CoFe_2O_4$–FH while the

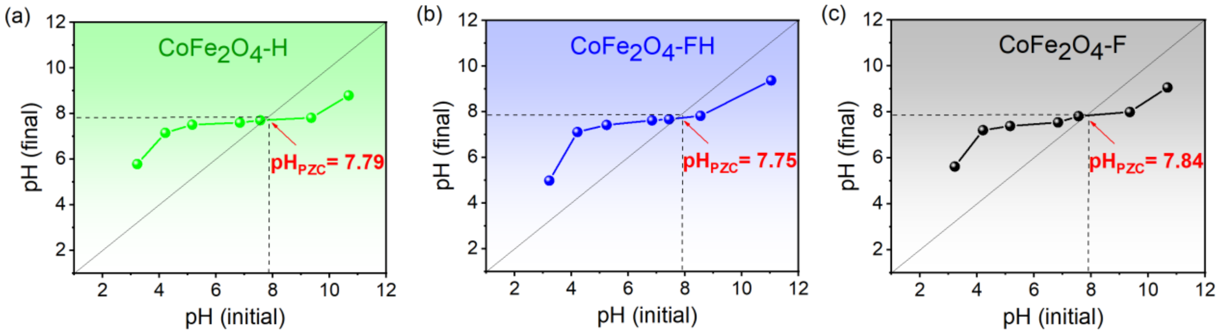

Fig. 7. Point of zero charges of $CoFe_2O_4$ samples, synthesized using the extracts of (a) husk (H), (b) fruit+husk (FH), and (c) fruit (F) of Physalis.

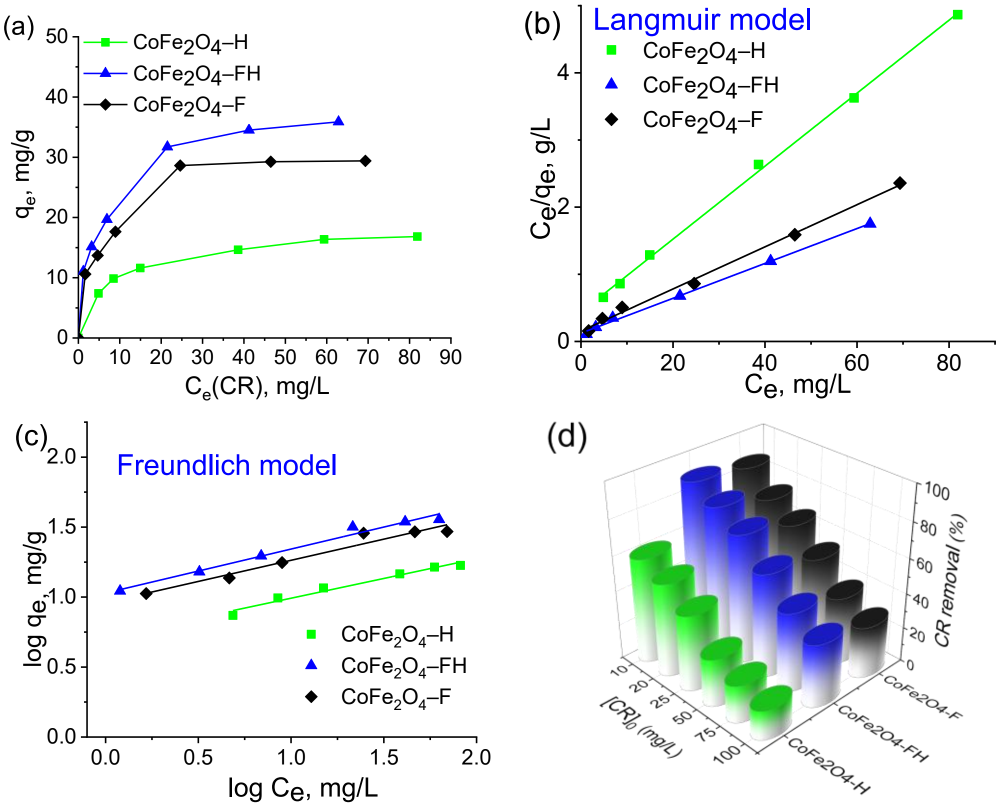

Fig. 8. Congo Red dye adsorption from the aqueous solutions using synthesized cobalt ferrites: (a) adsorption isotherms; (b) Langmuir model; (c) Freundlich model; (d) The FTIR-ATR spectra of $CoFe_2O_4$ samples after Congo red dye adsorption; (d) The percentage of CR dye removal (conditions: m (adsorbent) = 20 mg; V (solution) = 20 mL; C_0(CR) = 10; 20; 50; 75; 100 mg/L; T = 298 K).

Table 5.

The parameters of Langmuir and Freundlich models.

Sample	Adsorption model						
	Langmuir				Freundlich		
	q_{max}, mg/g	R^2	K_L, L/mg	R_L	R^2	K_F, (mg/g)(mg/L)^n	n
$CoFe_2O_4$–H	18.42	0.999	0.12	0.08	0.970	9.3	3.54
$CoFe_2O_4$–FH	38.46	0.998	0.21	0.05	0.980	10.7	3.18
$CoFe_2O_4$–F	31.85	0.996	0.20	0.05	0.953	9.13	3.31

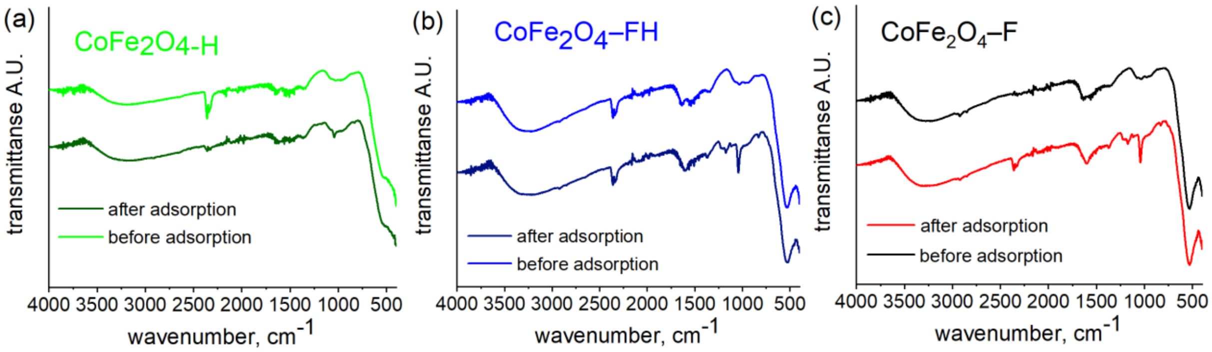

Fig. 9. The FTIR-ATR spectra of $CoFe_2O_4$ samples after Congo red dye adsorption.

lowest was for sample $CoFe_2O_4$–H.

Figs. 9a–c show the FTIR spectra of the $CoFe_2O_4$ samples after the CR adsorption. It can be seen that the bonds characteristic of the Congo Red dye molecule are prominently observed on the surfaces of $CoFe_2O_4$–F and $CoFe_2O_4$–FH samples, while they are less pronounced on the surface of $CoFe_2O_4$–H sample. The presence of dye residues on the surface of the adsorbent indicates the chemical nature of adsorption. A shift in the characteristic absorption wave of the O–H bonds in the range of 3600–3100 cm^{-1} is observed, which may indicate their participation in chemisorption. This is confirmed by the increase of peak intensities at 1596 cm^{-1} in the $CoFe_2O_4$–F and $CoFe_2O_4$–FH spectra, which indicate the deformation vibrations of water residues $\delta_{(HOH)}$. The region between 1360 cm^{-1} and 829 cm^{-1} contains typical bands for phenolic compounds and nitrogenous substances, such as the vibration of C–O, C–C, C–N, and C–H bonds [33,34].

The broad absorption band 1363 – 829 cm^{-1} for all three samples indicates the vibrations that belong to the aromatic –C=C– stretching vibration of the skeleton of the Congo Red molecule. A pronounced band at 1041 cm^{-1} signifies the S=O stretching vibration [38]. From the analysis of the IR spectra, it can be seen that adsorption is better on the surface of samples $CoFe_2O_4$–F and $CoFe_2O_4$–FH than on the surface of the $CoFe_2O_4$–H sample. In the sample $CoFe_2O_4$–H, not only is the adsorption capacity not significantly manifested but residual CO_2 has also been released, as evidenced by a decrease in the intensity in the corresponding part of the spectrum. IR spectra and percentage of the dye removal (Fig. 9c and Fig. 9d) show that adsorption is better on the surface with a higher degree of functionalization.

2.7. Fenton-like catalytic activity

The Fenton-like catalytic oxidation of Congo Red dye in the presence of H_2O_2 has been studied with and without a pre-adsorption stage. Figs. 10a–c and 11a–c show changes in the UV spectra of Congo Red solutions during both cases. The kinetic curves of the catalytic decomposition of Congo Red are presented in Figs. 10e and 11e. The data were analyzed using a first-order kinetics model (Figs. 10f and 11f), and the corresponding rate constants for each catalyst were calculated (Figs. 10g and 11g). It is clear that the catalytic activity of the samples is almost the same. The percentage of dye removal is presented in Figs. 10d and 11d. Fig. 10d shows that approximately half of the dye was adsorbed during the first 30 minutes (Fig. 10d). Both catalytic experiments were accompanied by the measurement of the residual hydrogen peroxide at the end of the experiments (Figs. 10h and 11h), and it was shown that in both cases the complete depletion of H_2O_2 was observed. Hydrogen peroxide interacts with the catalyst due to Fenton-like mechanism and undergoes decomposition to form hydroxyl ($^{\bullet}OH$) radicals [39]. This process occurs when Co(II) ions act as electron donors and hydrogen peroxide functions as an electron acceptor. The decomposition is represented by the following equation:

$Co^{2+} + H_2O_2 \rightarrow Co^{3+} + {}^{\bullet}OH + OH^{-}$.

The formed hydroxyl radicals subsequently attack the CR dye molecules through a Fenton-like degradation mechanism: CR dye + $^{\bullet}OH \rightarrow$ intermediates.

2.8. Electrochemical tests

The I–τ response curve provides a quantitative method for analyzing the electron transfer between ferrite catalysts and hydrogen peroxide enabling the assessment of catalytic efficiency and radical generation [40,41]. In the experiment, a galvanostat–potentiostat Autolab PGSTAT12 Eco Chemie was used for the measurements. The setup included a three-electrode system (see Section 2.4), which was allowed to reach equilibrium, and hydrogen peroxide was introduced into the electrolyte solution at the 100th second under continuous stirring [41].

Upon the catalytic decomposition of hydrogen peroxide, free radicals were generated in the solution, leading to a sudden increase in current on the I–τ curve (Fig. 12a). This current jump represents the electron transfer between the ferrite catalysts and hydrogen peroxide. By about 400th seconds, the system reached a steady state, and the current value at this point was recorded as the system's response. This value reflects the overall catalytic activity and the efficiency of electron transfer (Fig. 12b). Fig. 12b shows that current transmission increases in the following order:

$CoFe_2O_4$–F < $CoFe_2O_4$–FH < $CoFe_2O_4$–H. Fig. 12c shows the correlation between the current jump and the catalytic activity (taken from Fig. 10g). The catalytic activity after reaching adsorption equilibrium increases with increasing current jump.

The observed jumps in the electrochemical curves are primarily attributed to the interactions between hydrogen peroxide and the ferrite surface. In this context, the analysis of FTIR spectra is helpful. As depicted in Fig. 5a, the samples exhibit variations in the quantity of adsorbed carbon dioxide. This variation may result from the

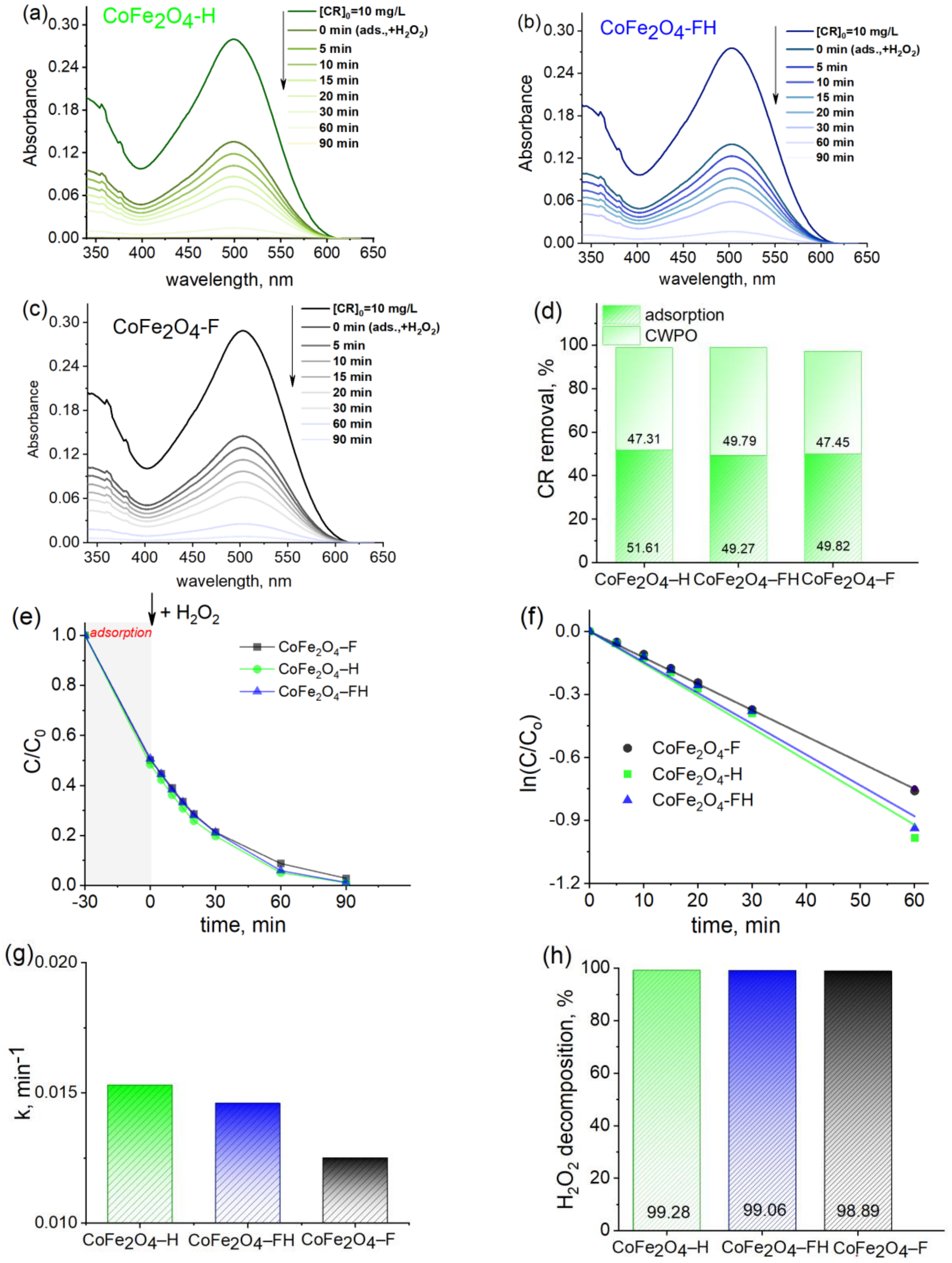

Fig. 10. The activity of cobalt ferrites in the catalytic experiments, including adsorption pre-stage: (a-c) the changes in UV–Vis spectra of CR solutions *vs.* time during the adsorption pre-stage; (d) the percentage of CR removal; (e) the kinetic curves of the CR catalytic oxidation; (f) the first-order kinetics model; (g) the values of the rate constants; (h) the H_2O_2 decomposition (conditions: m (catalyst) = 120 mg; V (solution) = 40 mL; C_0(CR) = 10 mg/L; T = 298 K; $C_0(H_2O_2)$ = 20 mM).

different amounts of surface cations, which could act as Lewis acids [42], presented on the ferrite surfaces. Considering that carbon dioxide could act as a Lewis base [43], it can be concluded that the highest amount of acid surface centers are presented in the sample $CoFe_2O_4$–H (Fig. 5a). Thus the plausible mechanism of the current jump (Fig. 12a) can be proposed. Hydrogen peroxide frequently functions as a Lewis base due to its ability to donate electrons, attributed to the presence of lone electron pairs on its oxygen atoms. This characteristic enhances its interactions with ferrite surfaces, particularly those rich in Lewis acid centers.

Additionally, the spinel structure provides greater accessibility to octahedral sites that are occupied by Co^{2+}

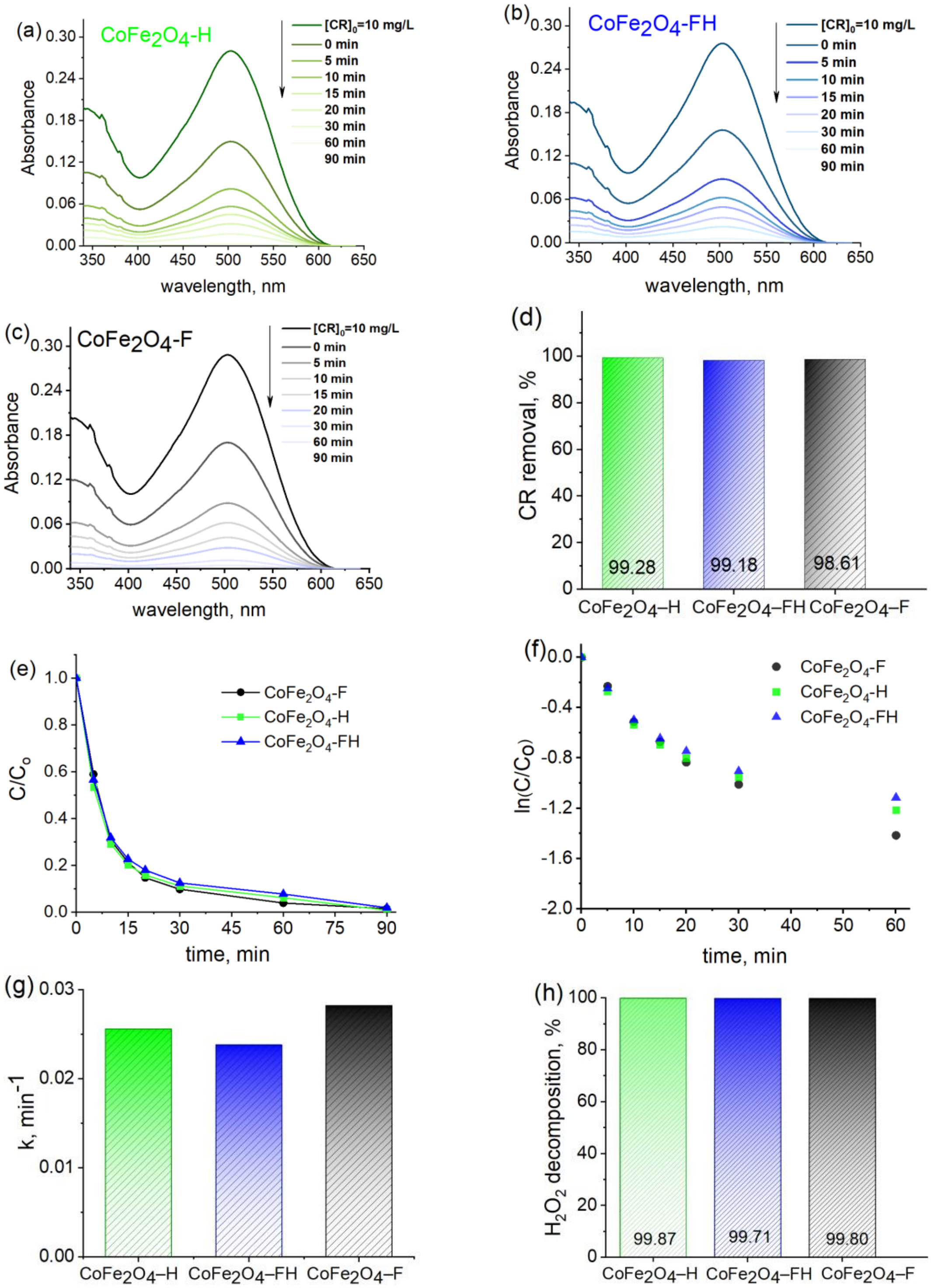

Fig. 11. The activity of cobalt ferrites in the catalytic experiments without adsorption pre-stage: (a-c) the changes in UV–Vis spectra of CR solutions *vs.* time; (d) the removal of CR dye (in %); (e) the kinetic curves of the CR catalytic oxidation; (f) the first-order kinetics model; (g) the values of the rate constants; (h) the H_2O_2 decomposition (conditions: m (catalyst) = 120 mg; V (solution) = 40 mL; C_0(CR) = 10 mg/L; T = 298 K; $C_0(H_2O_2)$ = 20 mM).

ions, which serve as Lewis acidic centers. These observations are consistent with the cation distribution of the analyzed samples. Notably, $CoFe_2O_4$–H demonstrates the highest amount of Co^{2+} ions within the B-sublattice (the highest inversion degree), which corresponds to the most significant increase in current observed in the I–τ curve, as illustrated in Fig. 12a. Organic residues on the surface of ferrite can also help break down hydrogen peroxide molecules. This process can change the amount of current carriers in the system and affect its electrical properties. The radicals produced during this breakdown can oxidize the organic residues. They compete with the dye molecules, leading to similar catalytic activities among the samples.

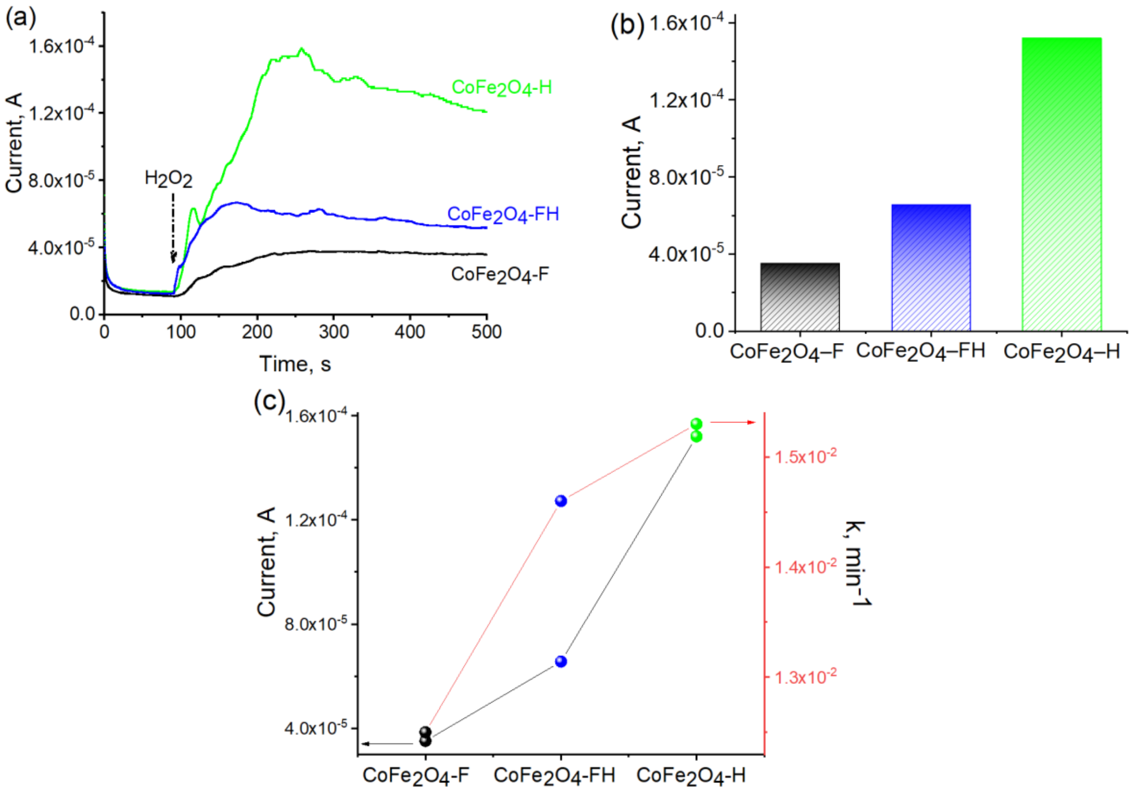

Fig. 12. (a) Amperometric I–τ curve measurements for cobalt ferrites: ([CR] = 10 mg/L; T = 298 K; [H_2O_2] = 20 mM). (b) The values of current transmission; (c) The correlation between the current transmission and the rate constants.

Conclusions

Magnetic nanoparticles of cobalt spinel ferrite were synthesized for the first time using biomaterial extracts of different parts of Physalis. As a result of the synthesis, spinel structure samples were obtained in all three cases, which was confirmed by X-ray analysis and confirmed by IR spectra. Using different parts of the plant bioreductant, it is possible to control the crystallite size and lattice parameter, the specific surface area, and the pore size of the nanoparticles. The presence of extract residues on the surface of the synthesized nanoparticles was confirmed by IR spectroscopic analysis. The choice of reducing agent (fuel) has a significant effect on the distribution of cations, the lattice parameter, and, as a result, the adsorption and catalytic properties. The adsorption capacity of the Congo Red dye is increased in the order $CoFe_2O_4$–H < $CoFe_2O_4$–F < $CoFe_2O_4$–FH. The Fenton-like catalytic activity of all three samples is notably high, although it is consistent across the samples. Electrochemical tests showed the significant increase in current observed in the I–τ curve for the $CoFe_2O_4$–H sample, related to its highest inversion degree (highest amount of Co^{2+} ions within the B-sublattice).

Acknowledgment

This work was supported by the Ministry of Education and Science of Ukraine (project number 0124U000479).

Liaskovska M.R. – assistant at Department of H.O. Babenko Biological and Medical Chemistry, Ivano-Frankivsk National Medical University; PhD student in Chemistry, Vasyl Stefanyk Precarpathian National University;
Tatarchuk T.R. – Associate Professor, PhD in Chemistry, Director of Educational and Scientific Center of Materials Science and Nanotechnology, Vasyl Stefanyk Precarpathian National University;
Kotsyubynsky V.O. –Professor, Doctor of Physical and Mathematical Sciences, Head of Department of Applied Physics and Materials Science, Vasyl Stefanyk Precarpathian National University.

[1] I. Khan, K. Saeed, I. Khan, *Nanoparticles: Properties, applications and toxicities*, Arab. J. Chem. (2019); https://doi.org/10.1016/j.arabjc.2017.05.011.
[2] P. Anastas, N. Eghbali, *Green chemistry: Principles and practice*, Chem. Soc. Rev. 39, 301 (2010); https://doi.org/10.1039/b918763b.

[3] N. Shreyash, S. Bajpai, M.A. Khan, Y. Vijay, S.K. Tiwary, M. Sonker, *Green Synthesis of Nanoparticles and Their Biomedical Applications: A Review*, ACS Appl. Nano Mater. 4, 11428 (2021); https://doi.org/10.1021/acsanm.1c02946.

[4] M. Liaskovska, T. Tatarchuk, M. Bououdina, I. Mironyuk, *Green Synthesis of Magnetic Spinel Nanoparticles,* in: Springer Proc. Phys., (2019). https://doi.org/10.1007/978-3-030-17755-3_25.

[5] M. Liaskovska, T. Tatarchuk, *Green synthesis of zinc ferrite*, Mol. Cryst. Liq. Cryst. 719, 45 (2021); https://doi.org/10.1080/15421406.2020.1862459.

[6] I.M. Chung, I. Park, K. Seung-Hyun, M. Thiruvengadam, G. Rajakumar, *Plant-Mediated Synthesis of Silver Nanoparticles: Their Characteristic Properties and Therapeutic Applications*, Nanoscale Res. Lett. 11, 1 (2016); https://doi.org/10.1186/s11671-016-1257-4.

[7] S. Gómez-Graña, M. Perez-Ameneiro, X. Vecino, I. Pastoriza-Santos, J. Perez-Juste, J.M. Cruz, A.B. Moldes, *Biogenic synthesis of metal nanoparticles using a biosurfactant extracted from corn and their antimicrobial properties*, Nanomaterials. 7 (2017); https://doi.org/10.3390/nano7060139.

[8] T. Tatarchuk, M. Liaskovska, V. Kotsyubynsky, M. Bououdina, *Green synthesis of cobalt ferrite nanoparticles using Cydonia oblonga extract: structural and mössbauer studies*, Mol. Cryst. Liq. Cryst. 672 (2018); https://doi.org/10.1080/15421406.2018.1542107.

[9] S.S.L. Ali, S. Selvaraj, K.M. Batoo, A. Chauhan, G. Rana, S. Kalaichelvan, A. Radhakrishnan, *Green synthesis of cubic spinel ferrites and their potential biomedical applications,* Ceram. Int. (2024); https://doi.org/10.1016/J.CERAMINT.2024.10.084.

[10] M. Madhukara Naik, H.S. Bhojya Naik, G. Nagaraju, M. Vinuth, K. Vinu, R. Viswanath, *Green synthesis of zinc doped cobalt ferrite nanoparticles: Structural, optical, photocatalytic and antibacterial studies,* Nano-Structures and Nano-Objects. 19, 100322 (2019); https://doi.org/10.1016/j.nanoso.2019.100322.

[11] D. Gingasu, I. Mindru, S. Preda, J.M. Calderon-Moreno, D.C. Culi, L. Patron, L. Diamandescu, *Green synthesis of cobalt ferrite nanoparticles using plant extracts*, Rev. Roum. Chim. 62, 645 (2017).

[12] M.K. Satheeshkumar, E.R. Kumar, C. Srinivas, N. Suriyanarayanan, M. Deepty, C.L. Prajapat, T.V.C. Rao, D.L. Sastry, *Study of structural, morphological and magnetic properties of Ag substituted cobalt ferrite nanoparticles prepared by honey assisted combustion method and evaluation of their antibacterial activity,* J. Magn. Magn. Mater. 469, 691 (2019); https://doi.org/https://doi.org/10.1016/j.jmmm.2018.09.039.

[13] R.S. Yadav, I. Kuřitka, J. Vilcakova, P. Urbánek, M. Machovsky, M. Masař, M. Holek, *Structural, magnetic, optical, dielectric, electrical and modulus spectroscopic characteristics of ZnFe2O4 spinel ferrite nanoparticles synthesized via honey-mediated sol-gel combustion method*, J. Phys. Chem. Solids. 110, 87 (2017); https://doi.org/https://doi.org/10.1016/j.jpcs.2017.05.029.

[14] K. Kombaiah, J.J. Vijaya, L.J. Kennedy, M. Bououdina, R.J. Ramalingam, H.A. Al-Lohedan, *Okra extract-assisted green synthesis of* $CoFe_2O_4$ *nanoparticles and their optical, magnetic, and antimicrobial properties*, Mater. Chem. Phys. 204, 410 (2018); https://doi.org/10.1016/j.matchemphys.2017.10.077.

[15] Y.P. Yew, K. Shameli, M. Miyake, N. Kuwano, N.B. Bt Ahmad Khairudin, S.E. Bt Mohamad, K.X. Lee, *Green Synthesis of Magnetite* (Fe_3O_4) *Nanoparticles Using Seaweed (Kappaphycus alvarezii) Extract,* Nanoscale Res. Lett. 11 (2016); https://doi.org/10.1186/s11671-016-1498-2.

[16] M. Madhukara Naik, H.S. Bhojya Naik, G. Nagaraju, M. Vinuth, H. Raja Naika, K. Vinu, *Green synthesis of zinc ferrite nanoparticles in Limonia acidissima juice: Characterization and their application as photocatalytic and antibacterial activities,* Microchem. J. 146, 1227 (2019); https://doi.org/10.1016/j.microc.2019.02.059.

[17] B.S. Surendra, *Green engineered synthesis of Ag-doped* $CuFe_2O_4$*: Characterization, cyclic voltammetry and photocatalytic studies,* J. Sci. Adv. Mater. Devices. 3, 44 (2018); https://doi.org/10.1016/j.jsamd.2018.01.005.

[18] D. Gingasu, I. Mindru, O.C. Mocioiu, S. Preda, N. Stanica, L. Patron, A. Ianculescu, O. Oprea, S. Nita, I. Paraschiv, M. Popa, C. Saviuc, C. Bleotu, M.C. Chifiriuc, *Synthesis of nanocrystalline cobalt ferrite through soft chemistry methods: A green chemistry approach using sesame seed extract,* Mater. Chem. Phys. 182, 219 (2016); https://doi.org/10.1016/j.matchemphys.2016.07.026.

[19] N. Mazova, V. Popova, A. Stoyanova, *Food Science and Applied Biotechnology Phytochemical composition and biological activity of Physalis spp.: A mini-review*, Food Sci. Appl. Biotechnol. 2020, 56 (2020).

[20] J. Ramakrishna Pillai, A.F. Wali, G.A. Menezes, M.U. Rehman, T.A. Wani, A. Arafah, S. Zargar, T.M. Mir, *Chemical Composition Analysis, Cytotoxic, Antimicrobial and Antioxidant Activities of Physalis angulata L.: A Comparative Study of Leaves and Fruit*, Molecules. 27 (2022); https://doi.org/10.3390/molecules27051480.

[21] L.-X. Chen, G.-Y. Xia, Q.-Y. Liu, Y.-Y. Xie, F. Qiu, *Chemical constituents from the calyces of Physalis alkekengi var. franchetii,* Biochem. Syst. Ecol. 54, 31 (2014); https://doi.org/https://doi.org/10.1016/j.bse.2013.12.030.

[22] C.-R. Zhang, W. Khan, J. Bakht, M.G. Nair, *New antiinflammatory sucrose esters in the natural sticky coating of tomatillo (Physalis philadelphica), an important culinary fruit,* Food Chem. 196, 726 (2016); https://doi.org/https://doi.org/10.1016/j.foodchem.2015.10.007.

[23] Y.-M. Xu, E.M.K. Wijeratne, A.D. Brooks, P. Tewary, L.-J. Xuan, W.-Q. Wang, T.J. Sayers, A.A.L. Gunatilaka, *Cytotoxic and other withanolides from aeroponically grown Physalis philadelphica*, Phytochemistry. 152, 174 (2018); https://doi.org/https://doi.org/10.1016/j.phytochem.2018.04.018.

[24] L.-X. Chen, G.-Y. Xia, H. He, J. Huang, F. Qiu, X.-L. Zi, *New withanolides with TRAIL-sensitizing effect from Physalis pubescens L.*, RSC Adv. 6, 52925 (2016); https://doi.org/10.1039/C6RA07031K.

[25] J.R. Medina-Medrano, N. Almaraz-Abarca, M.S. González-Elizondo, J.N. Uribe-Soto, L.S. González-Valdez, Y. Herrera-Arrieta, *Phenolic constituents and antioxidant properties of five wild species of Physalis (Solanaceae)*, Bot. Stud. 56, 24.(2015); https://doi.org/10.1186/s40529-015-0101-y.

[26] J. Qu, X. Yuan, X. Wang, P. Shao, *Zinc accumulation and synthesis of ZnO nanoparticles using Physalis alkekengi L.,* Environ. Pollut. 159, 1783 (2011); https://doi.org/https://doi.org/10.1016/j.envpol.2011.04.016.

[27] V. Sekar, M.M. Al-Ansari, J. Narenkumar, L. Al-Humaid, P. Arunkumar, A. Santhanam, *Synthesis of gold nanoparticles (AuNPs) with improved anti-diabetic, antioxidant and anti-microbial activity from Physalis minima*, J. King Saud Univ. -Sci. 34, 102197 (2022);https://doi.org/https://doi.org/10.1016/j.jksus.2022.102197.

[28] G.S. Vasyliev, V.I. Vorobyova, O.M. Kuzmenko, M.I. Skiba, *Electrochemical evaluation of reducing ability of plant extracts*, (n.d.) 246–267.

[29] A. Rondinone, A. Samia, Z. John, *Characterizing the magnetic anisotropy constant of spinel cobalt ferrite nanoparticles,* Appl. Phys. Lett. 76, 3624 (2000); https://doi.org/10.1063/1.126727.

[30] T. Tatarchuk, N. Danyliuk, A. Shyichuk, V. Kotsyubynsky, I. Lapchuk, V. Mandzyuk, *Green synthesis of cobalt ferrite using grape extract: the impact of cation distribution and inversion degree on the catalytic activity in the decomposition of hydrogen peroxide*, Emergent Mater. 5, 89 (2022).

[31] A.L. Tiano, G.C. Papaefthymiou, C.S. Lewis, J. Han, C. Zhang, Q. Li, C. Shi, A.M.M. Abeykoon, S.J.L. Billinge, E. Stach, J. Thomas, K. Guerrero, P. Munayco, J. Munayco, R.B. Scorzelli, P. Burnham, A.J. Viescas, S.S. Wong, *Correlating size and composition-dependent effects with magnetic, Mössbauer, and pair distribution function measurements in a family of catalytically active ferrite nanoparticles,* Chem. Mater. 27, 3572 (2015); https://doi.org/10.1021/acs.chemmater.5b00767.

[32] T. Tatarchuk, A. Shyichuk, V. Kotsyubynsky, N. Danyliuk, *Catalytically active cobalt ferrites synthesized using plant extracts: Insights into structural, optical, and catalytic properties,* Ceram. Int. 51, 4988 (2025); https://doi.org/https://doi.org/10.1016/j.ceramint.2024.11.470.

[33] N. Colthup, Introduction to infrared and Raman spectroscopy, Elsevier, 2012.

[34] D. Cozzolino, *The Role of Visible and Infrared Spectroscopy Combined with Chemometrics to Measure Phenolic Compounds in Grape and Wine Samples,* Molecules. 20, 726 (2015); https://doi.org/10.3390/molecules20010726.

[35] M. Thommes, K. Kaneko, A. V. Neimark, J.P. Olivier, F. Rodriguez-Reinoso, J. Rouquerol, K.S.W. Sing, *Physisorption of gases, with special reference to the evaluation of surface area and pore size distribution (IUPAC Technical Report),* Pure Appl. Chem. 87, 1051 (2015); https://doi.org/10.1515/pac-2014-1117.

[36] D.H.K. Reddy, Y.-S. Yun, *Spinel ferrite magnetic adsorbents: Alternative future materials for water purification?*, Coord. Chem. Rev. 315, 90 (2016); https://doi.org/10.1016/J.CCR.2016.01.012.

[37] M. Liaskovska, *Adsorption Properties of Magnetic $CoFe_2O_4$ Based Spinel Nanoparticles,* Nanomater. Nanocomposites, Nanostructures, Their Appl. (2024); https://doi.org/10.1007/978-3-031-67519-5_13.

[38] C. Aoopngan, J. Nonkumwong, S. Phumying, W. Promjantuek, S. Maensiri, P. Noisa, S. Pinitsoontorn, S. Ananta, L. Srisombat, *Amine-Functionalized and Hydroxyl-Functionalized Magnesium Ferrite Nanoparticles for Congo Red Adsorption*, ACS Appl. Nano Mater. 2, 5329 (2019); https://doi.org/10.1021/acsanm.9b01305.

[39] T. Tatarchuk, *Studying the Defects in Spinel Compounds: Discovery, Formation Mechanisms, Classification, and Influence on Catalytic Properties,* Nanomaterials. 14 (2024); https://doi.org/10.3390/nano14201640.

[40] J. Hu, X. Zeng, G. Wang, B. Qian, Y. Liu, X. Hu, B. He, L. Zhang, X. Zhang, *Modulating mesoporous Co_3O_4 hollow nanospheres with oxygen vacancies for highly efficient peroxymonosulfate activation*, Chem. Eng. J. 400 125869 (2020); https://doi.org/https://doi.org/10.1016/j.cej.2020.125869.

[41] M. Liaskovska, T. Tatarchuk, V. Kotsyubynsky, *Green Synthesis of Cobalt–Zinc Ferrites and Their Activity in Dye Elimination via Adsorption and Catalytic Wet Peroxide Oxidation,* Metals (Basel). 15 (2025); https://doi.org/10.3390/met15010044.

[42] J. Kim, B.B. Sarma, E. Andrés, N. Pfänder, P. Concepción, G. Prieto, *Surface Lewis Acidity of Periphery Oxide Species as a General Kinetic Descriptor for CO_2 Hydrogenation to Methanol on Supported Copper Nanoparticles*, ACS Catal. 9, 10409 (2019); https://doi.org/10.1021/acscatal.9b02412.

[43] A. Zecchina, C. Lamberti, S. Bordiga, *Surface acidity and basicity: General concepts*, Catal. Today. 41, 169 (1998). https://doi.org/https://doi.org/10.1016/S0920-5861(98)00047-9.

Марія Лясковська[1,2], Тетяна Татарчук[3], Володимир Коцюбинський[4]

Структура, адсорбційні властивості та Фентон-подібна каталітична активність наночастинок фериту кобальту, синтезованих з екстрактом фізалісу

[1] Івано-Франківський національний медичний унверситет, Івано-Франківськ, Україна; mliaskovska@ifnmu.edu.ua
[2] Кафедра хімії, Прикарпатський національний університет імені Василя Стефаника, Івано-Франківськ, Україна; liaskovskam@gmail.com
[3]Навчально-науковий центр хімічного матеріалознавства та нанотехнологій, Прикарпатський національний університет імені Василя Стефаника, Івано-Франківськ, Україна
[4]Кафедра прикладної фізики і матеріалознавства, Прикарпатський національний університет імені Василя Стефаника, Івано-Франківськ, Україна; volodymyr.kotsuybynsky@pnu.edu.ua

Наночастинки фериту кобальту синтезовані з різних частин екстракту фізалісу. Методи визначення характеристик, включаючи Х-променевий аналіз та дані ІЧ-спектроскопії, підтвердили структуру шпінелі синтезованих феритів. Згідно з даними ІЧ, спектри містять піки, що відповідають органічним залишкам, які походять від «зеленого» відновника. Дані Х-променевого аналізу свідчать про збільшення параметра гратки та розміру кристалітів у ряду: $CoFe_2O_4$–F < $CoFe_2O_4$–FH < $CoFe_2O_4$–H. Відповідно до фотографій СЕМ, зразок $CoFe_2O_4$–H демонструє нижчий ступінь агломерації в поєднанні зі значною пористістю, тоді як $CoFe_2O_4$–FH та $CoFe_2O_4$–F зразки демонструють більш чіткі пластинчасті структури. Ступінь інверсії розраховували на основі мессбауерівських спектрів зразків. Дані БЕТ показують, що використання екстракту плодів фізалісу+лушпиння призводить до утворення наночастинок зі збільшеною площею поверхні (76 $м^2/г$), а використання екстракту плодів фізалісу призводить до утворення збільшеної площі мезопор (46 $м^2/г$). Досліджено адсорбційні та Фентон-подібні каталітичні властивості синтезованих зразків. Найвищий ступінь видалення барвника Конго Червоного спостерігався для зразка $CoFe_2O_4$–FH, тоді як найнижчий для $CoFe_2O_4$–H. ІЧ-спектри підтвердили хемосорбцію молекул барвника на поверхні фериту. Адсорбція вища на поверхні з вищим ступенем функціональності. Досліджено Фентон-подібне каталітичне окислення барвника Конго Червоного у присутності H_2O_2, що продемонструвало високу каталітичну активність усіх зразків щодо видалення барвника та розкладання пероксиду водню. Амперометричні вимірювання кривої I–τ використовували для спостереження змін у взаємодії між пероксидом водню та феритами.

Ключові слова: “зелений” синтез; ферит; адсорбція; Фентон-подібна активність; електрохімічний тест; окиснювальна деградація.